small methods
www.small-methods.com

Knot Architecture for Biocompatible and Semiconducting 2D Electronic Fiber Transistors

Tian Carey, Jack Maughan, Luke Doolan, Eoin Caffrey, James Garcia, Shixin Liu, Harneet Kaur, Cansu Ilhan, Shayan Seyedin, and Jonathan N. Coleman**

Wearable devices have generally been rigid due to their reliance on silicon-based technologies, while future wearables will utilize flexible components for example transistors within microprocessors to manage data. Two-dimensional (2D) semiconducting flakes have yet to be investigated in fiber transistors but can offer a route toward high-mobility, biocompatible, and flexible fiber-based devices. Here, the electrochemical exfoliation of semiconducting 2D flakes of tungsten diselenide (WSe_2) and molybdenum disulfide (MoS_2) is shown to achieve homogeneous coatings onto the surface of polyester fibers. The high aspect ratio (>100) of the flake yields aligned and conformal flake-to-flake junctions on polyester fibers enabling transistors with mobilities $\mu \approx 1$ cm^2 V^{-1} s^{-1} and a current on/off ratio, $I_{on}/I_{off} \approx 10^2$–$10^4$. Furthermore, the cytotoxic effects of the MoS_2 and WSe_2 flakes with human keratinocyte cells are investigated and found to be biocompatible. As an additional step, a unique transistor 'knot' architecture is created by leveraging the fiber diameter to establish the length of the transistor channel, facilitating a route to scale down transistor channel dimensions (≈100 µm) and utilize it to make a MoS_2 fiber transistor with a human hair that achieves mobilities as high as $\mu \approx 15$ cm^2 V^{-1} s^{-1}.

1. Introduction

There is an increasing trend toward incorporating technology into the clothes we wear. In just the last thirty years, over two-thirds of the world population have begun to carry a smartphone in their pocket,[1] and there is a growing demand for wearable devices with similar functionality.[2] However, many wearable technologies are still in their infancy and are based on rigid, bulky silicon components that were never initially intended for use with textile or fiber substrates.[2] Therefore, new protocols, materials, and device architectures will be needed to manufacture next-generation wearables so that the electronic devices can meet the stringent requirements of textile and fiber substrates, such as breathability, biocompatibility, flexibility, comfort, washability, and conformability of the components to the textile substrate.[3] Wearable technology will transition from glasses, bands, and watches to seamlessly embedded technology such as conformable fibers, textiles, tattoos, or implantable devices that will have features such as disease monitoring,[4] motion tracking,[5] thermal regulation,[6] lighting,[7] and energy harvesting components (e.g. photovoltaics, triboelectric, piezoelectric, and thermoelectric nanogenerators).[8–10] In many of these applications, transistors will be used as an active data collection component or as part of a microprocessor to analyze data.[4]

Textile transistors can be made as planar structures on textiles[11] or along single fibers or fibrils.[12] Manufacturing transistors on fibers is attractive but can be more challenging, often requiring transistor components smaller than the fiber diameter (<500 µm).[3] However, fiber-based devices can benefit from their 3D structure, which permits the possibility of novel device architectures,[13] compatibility with current textile manufacturing processes, and integration into multifunctional coaxial systems capable of performing multiple tasks simultaneously within a single fiber (e.g. energy generation and sensing).[14] Fiber transistors have been demonstrated with organic conducting polymers (e.g. poly(3,4-ethylenedioxythiophene) polystyrene sulfonate, PEDOT:PSS, and poly(3-hexylthiophene), P3HT),[12,15–17] semiconducting carbon nanotubes,[18] and metal oxides (e.g. indium–gallium–zinc oxide, IGZO).[19,20] Electrochemical fiber transistors are typically assembled using a shadow mask for metal evaporation to define the channel length (L_c) between electrodes.[20,21] Semiconductors are coated over the electrodes of the electrochemical fiber transistor and ionic liquid is drop cast onto the semiconducting channel to enable gating of the device.[22] In contact with the ionic liquid, a metal wire is often

T. Carey, J. Maughan, L. Doolan, E. Caffrey, J. Garcia, S. Liu, H. Kaur, C. Ilhan, J. N. Coleman
School of Physics
CRANN & AMBER Research Centers
Trinity College Dublin
Dublin Dublin 2, Ireland
E-mail: careyti@tcd.ie; colemaj@tcd.ie

S. Seyedin
School of Engineering
Newcastle University
Newcastle upon Tyne NE1 7RU, UK

The ORCID identification number(s) for the author(s) of this article can be found under https://doi.org/10.1002/smtd.202301654

DOI: 10.1002/smtd.202301654

used as the gate electrode.[15,21] Maskless approaches have also been used to define the source and drain electrodes through the mechanical weaving of metal fiber.[15] Removing the lithography manufacturing step has a cost reduction advantage however, it is difficult to form a narrow $L_c < 0.5$ mm which is needed for higher transistor performance and integration density.[15,23] Field effect transistors (FETs) are typically assembled by using a metal wire to define a gate,[24–27] which is then coated with a dielectric material (e.g. aluminum oxide, parylene C) by evaporation.[24–26,28] The semiconductor is then evaporated, coated, or drop-cast onto the dielectric.[24–29] Like electrochemical devices, metal evaporation through a shadow mask defines source and drain electrodes. The performance of the fiber transistors ranges from mobilities $\mu \approx 0.001$–1.7 cm^2 V^{-1} s^{-1} with $I_{on}/I_{off} \approx 10^3$–$10^4$ for organic conducting polymers,[25–30] $\mu \approx 0.5$ cm^2 V^{-1} s^{-1} and $I_{on}/I_{off} \approx 10^4$ for single-walled carbon nanotubes (SWCNT)[18] and $\mu \approx 1.5$–5.5 cm^2 V^{-1} s^{-1} and $I_{on}/I_{off} \approx 10^4$–$10^7$ for IGZO.[19,20,31,32] SWCNT transistors have excellent resilience to tensile strain >3% but it is difficult to isolate semiconducting SWCNT during production which can drive the cost >$1000 per gram.[33,34] IGZO has demonstrated some of the best performances to date however, the μ decreases significantly to <0.1 cm^2 V^{-1} s^{-1} at <0.1% tensional strain making it challenging to implement in wearable products.[19] Organic conducting polymers such as P3HT do not suffer a μ drop with high strain (30–50%).[30] However, after several decades of research, they have reached a performance plateau $\mu \approx 10$ cm^2 V^{-1} s^{-1}, even in planar thin films.[35]

Transition metal dichalcogenides (TMD) flakes offer enormous potential and a new route forward in the development of fiber transistors offering a significant number of advantages such as flexibility,[11] durability,[5] minimal toxicity,[36] and transistors with flake networks having $\mu > 10$ cm^2 V^{-1} s^{-1}.[37,38] Furthermore, TMD flakes can be made by liquid phase exfoliation (LPE) or electrochemical exfoliation (EE) and processed into the form of inks that can be readily applied on demand and provide benefits such as low-temperature processing (<120 °C), form factor benefits (e.g., easy to apply on rough >1 µm textile surfaces), lower production costs compared to growth methods,[39] and scalability.[40] Despite high mobility in the basal plane of the LPE 2D flakes,[41] inter-flake junctions have typically limited the flake network μ,[42] leading to low μ <0.3 cm^2 V^{-1} s^{-1}.[43,44] A new method of EE has recently emerged to produce large (aspect ratio, AR >100) semiconducting 2D flakes using quaternary ammonium salts (QAS).[38] The flakes can be used to create conformal flake networks that are limited by the quality of the 2D flake basal plane, enabling a route for network $\mu > 10$ cm^2 V^{-1} s^{-1}.[37,42] However, to our knowledge, fiber-based transistors with semiconducting flakes are yet to be achieved despite the tremendous potential. Furthermore, the biocompatibility of flakes made by QAS is largely unknown but extremely important if implemented in electronic fiber applications that could encounter human cells (e.g. electrodes, sensors, and thermal interface components).

This work will demonstrate the effect of EE with MoS_2 and WSe_2 flakes on cytotoxicity with human skin cells to enable the use of 2D flakes in wearable applications. We will use EE flakes with polyester fibers to make conformal junctions and realize high μ WSe_2 and MoS_2 fiber transistors. Additionally, we will demonstrate a methodology to make fiber transistors with a short L_c <200 µm without the need for lithography masks, to facilitate cost reduction, increase device density, and enable a more straightforward manufacturing process toward high-performance fiber transistors.

2. Results

2.1. Electrochemical Exfoliation of TMD Flakes

We use EE to intercalate and expand bulk crystals of MoS_2 and WSe_2 using QAS in propylene carbonate (see Experimental Section). The expanded crystals are ultrasonicated in a dispersion of poly(vinylpyrrolidone)/dimethylformamide (PVP/DMF) and subsequently centrifuged at 97g to remove the unexpanded crystal. Next, centrifugation washing and solvent exchange were used to transfer the MoS_2 and WSe_2 flakes to isopropyl alcohol (IPA) to make our MoS_2 and WSe_2 ink, as described in the Experimental Section. IPA was chosen as it is a low boiling point solvent (≈82.5 °C), which will evaporate away quickly once deposited on the polyester fiber.[45]

In **Figure 1a**, we investigate the structure of the MoS_2 and WSe_2 flakes using X-ray diffraction (XRD) undertaken on drop-cast flake networks on silicon/silicon dioxide (Si/SiO_2) substrate. Both MoS_2 (green curve) and WSe_2 (brown curve) show diffraction peaks attributed to the 2H semiconducting phase of each material.[46–48] Two diffraction peaks located at 33° and 69° are also seen which we attribute to the silicon substrate.[49] Raman spectroscopy is used to determine the phase of the flakes in Figure 1b. Drop cast flake networks of MoS_2 (green curve) and WSe_2 (brown curve) showed the A_{1g} and E_{2g} Raman modes as expected[50,51] and are consistent with previous reports of 2H semiconducting flakes. The J2 and J3 vibration modes attributed to the metallic 1T phase (located at 224 and 289 cm^{-1} for MoS_2 and 218 and 236 cm^{-1} for WSe_2) are absent.[52,53]

We estimate the lateral flake size (L) and flake apparent thickness (t) using atomic force microscopy (AFM) statistics (See Experimental Section). Figure 1c plots L versus t for individual MoS_2 and WSe_2 flakes and no apparent correlation is observed. The average flake lateral size $\langle L \rangle$ is 2.3±0.1 µm and 1.20±0.02 with an average apparent flake thickness $\langle t \rangle$ of 9.7±0.2 nm and 17.4±0.5 nm for MoS_2 and WSe_2 respectively. Figure 1d is an AFM micrograph with an associated cross-section of a WSe_2 flake. Therefore, the average flake aspect ratio ($\langle AR \rangle$, $\langle L \rangle / \langle t \rangle$) is 251 and 98 for MoS_2 and WSe_2, respectively. These values are higher than the minimum AR required to make conformal flake-to-flake junctions (AR >40) which should also permit the flakes to wrap around fibers once deposited.[42]

Optical extinction, absorption, and scattering spectra of the MoS_2 and WSe_2 inks are presented in Figure 1e. Each spectrum shows the appropriate features with an A exciton at ≈676 and 772 nm for MoS_2 and WSe_2, respectively, consistent with previous reports of LPE and EE flakes.[37,54,55] The scattering component of the ink is ≈50% of the extinction spectra intensity and would suggest that the flakes have a large L.[54] Transmission electron microscopy (TEM) shown in Figure 1g,h also confirms the presence of large $L > 1$ µm flakes in the MoS_2 and WSe_2 inks.

2.2. Electrochemically Gated TMD Fiber Transistors

Next, we test the performance of the semiconducting TMD inks by fabricating electrochemically gated fiber transistors. Most

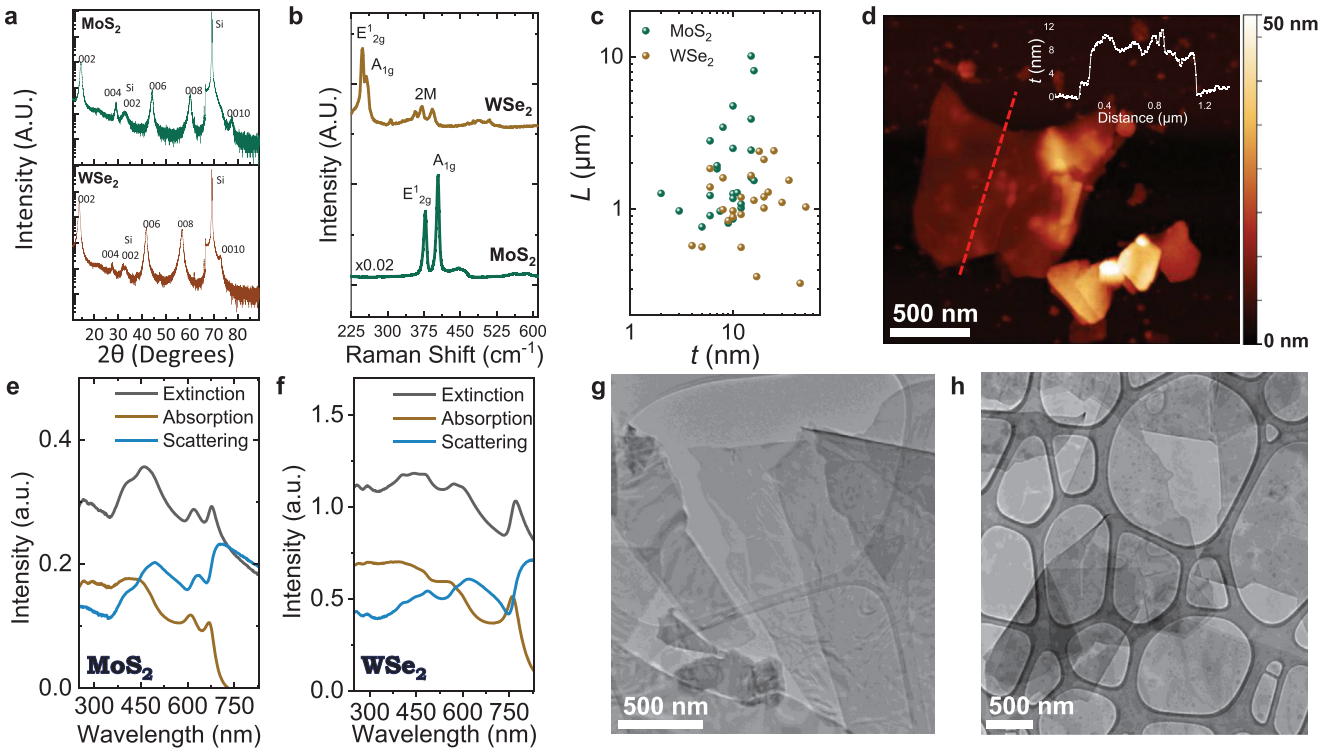

Figure 1. Electrochemical Exfoliation of TMDs. a) XRD of the TMDs flakes demonstrating the semiconducting (2H phase) of the materials. b) Raman spectroscopy chemical analysis of the TMDs following centrifugation into inks. c) Atomic force microscopy statistics of the flake lateral size and thickness. d) Atomic force microscopy micrograph of a representative WSe_2 flake. e,f) UV–vis optical analysis of the TMD inks demonstrating the extinction, absorption, and scattering components as a function of wavelength for the MoS_2 and WSe_2 ink. g,h) Transmission electron microscopy images of the MoS_2 and WSe_2 flakes showing $L > 1$ μm, flake fold and wrinkles.

fiber transistor literature uses evaporation to deposit the semiconducting layer,[25,26,28,30] requiring the rotation of the fiber for complete coverage. Here, the TMD inks have a form factor benefit, as the fiber does not need to be rotated during deposition, maximizing the process' potential scalability. The low surface tension (<30 mN m^{-1}) and low boiling point (<80 °C) of the TMD inks improve the morphological uniformity of the deposition. The low surface tension helps the ink spread along the fiber's surface, while the low boiling point permits the solvent to evaporate quickly at the point of deposition.[45] The MoS_2 and WSe_2 inks are drop cast (≈140 μL, ≈2 mg mL^{-1}) onto separate polyester fibers (Axel Suijker Textil, ⌀ ≈200 μm fiber diameter), composed of several hundred fibrils ($⌀_f$ ≈10 μm fibril diameter) to assist capillary action coating along the fiber (See Supporting Information). There are ≈400 fibrils per fiber ($(⌀/⌀_f)^2$). The MoS_2 and WSe_2 semiconducting fibers are created by annealing the coated fibers at 120 °C for 1 h on a hot plate in an N_2 glovebox to remove residual solvent and improve the adhesion of the MoS_2 and WSe_2 flake networks to polyester. In **Figure 2a**, scanning electron microscopy (SEM) imaging of the surface of the coated fibril reveals a highly aligned network of MoS_2 nanosheets, with conformal junctions between the flakes. Such conformal junctions are extremely important as they imply low junction resistance. It is worth noting that this is an important result as it implies that high aspect ratio semiconducting nanosheets prefer to lie flat if it is possible and do not need special deposition conditions (e.g. Langmuir–Schaeffer deposition),[37] to enable them to align. This is a result of favorable balance of van der Waals binding energy versus bending energy[42] which enables high aspect ratio nanosheets to conform to their neighbors. In Figure 2b, cross-sectional SEM also reveals that the MoS_2 network of flakes has coated the circumference of the fibrils while the inside of the polyester fibrils remains uncoated, insulating, and therefore bright in the SEM. Focused-ion beam SEM (FIB-SEM) imaging (see Experimental Section) shown in Figure 2c determines a flake network thickness, $t_c = 242 \pm 24$ nm around the fiber circumference. The mechanical properties of the semiconducting fibers are tested in Figure 2d, which show s that a similar stress–strain curve is obtained for both coated and uncoated fibers. An elastic modulus (slope of the stress–strain curve) of 0.57 ± 0.04, 0.31 ± 0.04, and 0.43 ± 0.13 GPa is found for the polyester (black curve), MoS_2/polyester (green curve), and WSe_2/polyester (brown curve) fibers respectively which is similar to previous reports for polyester fibers.[56] We define the strain at break as the onset of the pull-out regime (i.e. the point at which some fibrils start to break and the deformation is no longer elastic). We find that the strain at break is 4.3 ± 0.7, 3.2 ± 0.4, and 4 ± 1.0% for the polyester (black curve), MoS_2/polyester (green curve), and WSe_2/polyester (brown curve) fibers, respectively. These mechanical performances are the same within error. Therefore, the MoS_2 and WSe_2 flake networks are not significantly changing the mechanical properties of the polyester

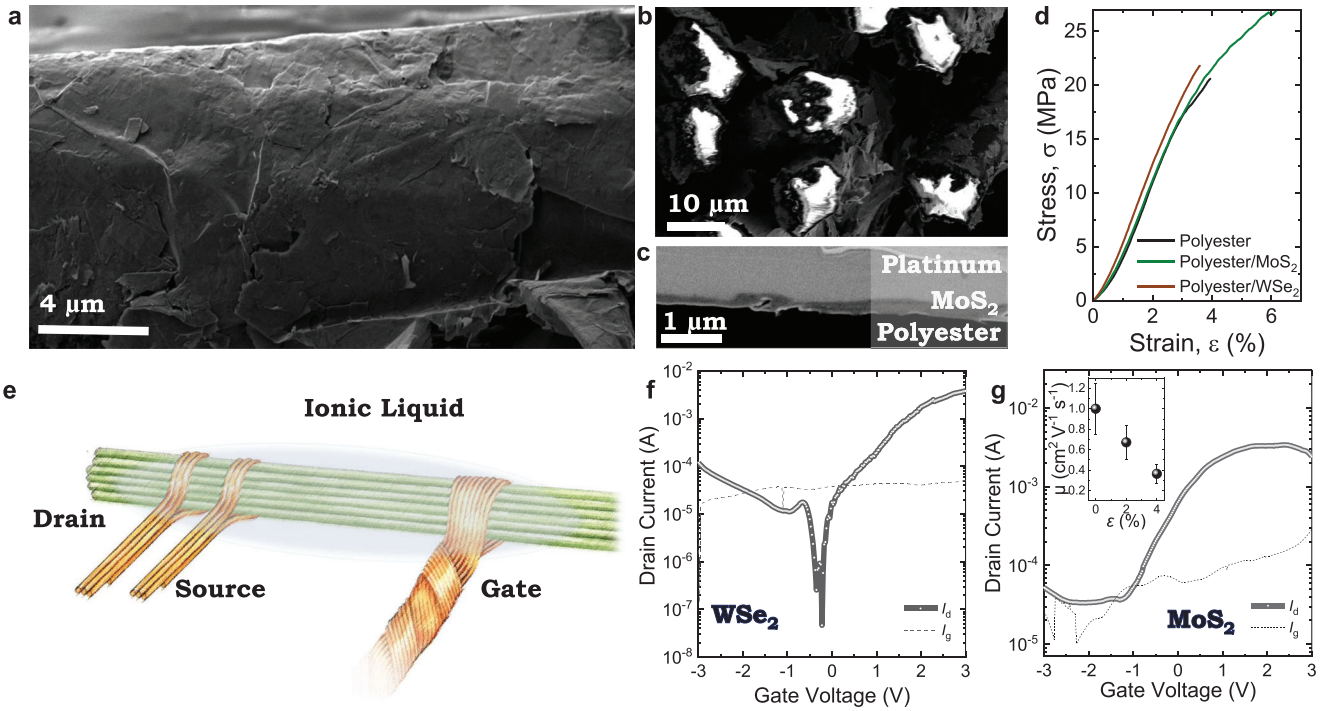

Figure 2. Investigation of fiber morphology and electrical properties. a) SEM of a MoS_2 coated MoS_2 fiber demonstrating conformal junctions and morphologically uniform coating. b) Cross-sectional SEM of the MoS_2 coated polyester fiber showing that each fibril has an MoS_2 flake coating and an uncoated interior c) SEM-FIB of an MoS_2 coated fibril. d) Mechanical testing of the TMD coated fibers. e) Schematic of fiber transistor showing the MoS_2 coated fibers in green and the copper electrodes in brown. f) Transfer characteristics of the WSe_2 and g) MoS_2 coated fibers with the gate leakage shown as a dashed line. The μ as a function of tensile strain on the MoS_2 coated fiber is shown in the inset. Error is calculated by fractional propagation of error (see Experimental Section).

fiber. We assemble a fiber transistor by manually wrapping copper wire ($\varnothing$ = 100 μm) around the bundle of semiconducting fibers to define the source and drain electrodes. We also add a copper side-gate by wrapping a copper electrode ≈1 cm from the channel, as shown in Figure 2e. The side gate is made of ≈10 copper wires manually wound together to create an active diameter of ≈1 mm. The gate is thicker than the source and drain electrodes, as previous work has shown that μ of ionic gated devices in 2D flake networks can be maximized when the gate volume is >10 times larger than the channel volume.[43] To complete our electrochemical transistor, shown in Figure 2e, we add a drop-cast ionic liquid (≈50 μL) 1-ethyl-3-methylimidazolium bis(trifluoromethylsulfonyl)imide (EMIM TFSI) to allow gating of the semiconducting channel.[22] The electrochemical transistors are then characterized using a probe station in ambient air. In Figure 2f,g, we sweep a gate voltage (V_g) from −3 to 3 V and apply a drain-source voltage, V_{ds} = 1 V, to obtain the transfer characteristics for the WSe_2 and MoS_2 transistors, respectively. In Figure 2f, the WSe_2 curve demonstrates ambipolar behavior with an off state at V_g ≈0 V while the MoS_2 transistor (Figure 2g) is n-type because the device turns off at negative V_g, confirming the electrical behavior is as expected and consistent with previous reports for TMD flake networks on polyethylene terephthalate (PET).[37] We also observe that the gate leakage, I_g attributed to the conductivity of the ionic liquid, is minimal (< 0.1 mA). The μ of the transistors is calculated from the equation $\mu = (L_c/W)(1/C_{device})(g_m/V_{ds})$, where $g_m = \partial I_d/\partial V_g$ is the transconductance, and C_{device} is the device capacitance. We have 400 fibrils in the channel with source and drain electrodes separated by a channel length L_c ≈400 ± 100 μm. For each fibril, their contribution to the channel width is the circumference of the fibril ($\pi\varnothing_f$), therefore $W = n\pi\varnothing_f$ where n is the number of fibrils. Our previous work has estimated an average volumetric capacitance, C_v ≈1.4 F cm^{-3} for networks of MoS_2 and WSe_2 nanosheets with similar thickness to those used here.[37] Using a flake network thickness t_c = 242 ± 24 nm, we can estimate $C_{device} = C_v \times t_c$ ≈33.9 μF cm^{-2}. Therefore, the average electron μ for MoS_2 and WSe_2 is calculated to be μ_{MoS2} ≈1 ± 0.3 cm^2 V^{-1} s^{-1} and μ_{WSe2} ≈1 ± 0.4 cm^2 V^{-1} s^{-1} with I_{on}/I_{off} ≈10^2 and ≈10^4 for MoS_2 and WSe_2 respectively. Notably, the MoS_2 I_{on}/I_{off} is significantly lower than the WSe_2. We attributed the low I_{on}/I_{off} of MoS_2 to a high I_d (≈ 10^{-5} A) in the I_{off} state, primarily due to unintentional doping, likely occurring during the EE process. We find the charge carrier density (n) from the formula $\sigma = nq\mu$ where q is the elemental charge and σ is the network conductivity. Our MoS_2 has n 10^{22}-10^{23} m^{-1} consistent with other work on EE of MoS_2 with ammonium salts.[38,57] The increased n results in an increase in charge screening and a decrease in I_{on}/I_{off}, which is also consistent with other reports of EE MoS_2 transistors with I_{on}/I_{off} <10^2.[58,59] For our WSe_2 network where n ≈10^{18} m^{-3}, we observe I_{on}/I_{off} > 10^4, partially due to a reduction in unintentional doping. As an additional step we test the flexibility of the MoS_2 fiber transistor by bending it at a fixed bending radius between 2.5 - 5mm (see Experimental Section) which varies the tensile strain, shown in the inset of Figure 2g.

We find μ decreases to 0.3 $cm^2\ V^{-1}\ s^{-1}$ at 4% tensile strain but remained operational.

The μ of our TMD fiber transistors is greater than the majority of organic conducting polymer and semiconducting carbon nanotube fiber transistors with comparable I_{on}/I_{off}[18,25–30] and slightly less than IGZO fibers $\mu \approx 1.5–5.5\ cm^2\ V^{-1}\ s^{-1}$ but with greater resilience to fiber strain (≈4%), an essential requirement for fiber electronics.[19,20,31,32] To our knowledge, electronic fibers with TMDs have not been achieved to date demonstrating an important first step. We attributed the reduction of the μ compared to planar devices on PET and Si/SiO_2 ($\mu > 10\ cm^2\ V^{-1}\ s^{-1}$) to the increased roughness of the fibrils and possible parasitic resistance in the channel created by the thick semiconducting layer $t_c = 242$ nm.[37,38]

2.3. Knotted Fiber TMD Transistor

To establish a route toward higher-performance fiber transistors ($\mu > 10\ cm^2\ V^{-1}\ s^{-1}$), patterning the source and drain electrodes needs a long-term strategy to decrease L_c and W to < 500 µm for increased integration density, to facilitate cost reduction and to enable a straightforward manufacturing process without the need for lithography, which traditionally has never been intended for use with fibers transistors. Kim et al. have used a twisted fiber assembly to overcome the difficulties of forming a narrow gap between source and drain electrodes. Gold fiber is coated with P3HT, and the coated fibers are twisted together to make L_c as low as 120 nm achieving $\mu \approx 0.2\ cm^2\ V^{-1}\ s^{-1}$.[17] However, getting short channel $W < 4$ cm in this configuration can be difficult.[17] Cross-bar geometry has also been used with a PEDOT:PSS coated polyamide fiber as the source, drain, and semiconductor channel as one fiber, and a second PEDOT:PSS coated fiber is positioned perpendicularly as the gate electrode.[12] While the L_c and W are defined by the gate fiber diameter ≈10 µm achieving $g_m \approx 10^{-4}$ S, the strategy is not viable for TMD materials where the semiconductor conductivity is too low $\approx 10^{-5}–10^{0}\ S\ m^{-1}$ to be used as a source-drain electrode.[12]

We demonstrate a new architecture to fabricate the fiber transistors, which use the fiber diameter (⌀ ≈200 µm) to define W and L_c. In **Figure 3a**, we use an overhand knot to wrap the semiconducting MoS_2-coated fiber around a copper wire (⌀ = 100 µm) to define the drain. Next, a second overhand knot is used to position the source. A force (F) is applied by hand in the direction of the arrows to tighten the MoS_2-coated fiber around the source and drain electrodes. As a result, the source-drain electrodes do not short-circuit since the MoS_2-coated fiber is between them. Assuming the current will only flow from the copper source to the drain through the fiber, we define $L_c = 2\times⌀ = 400$ µm, twice the fiber diameter, and $W = n\pi⌀_f = 12.57$ mm. Next, we add a copper side gate by wrapping a copper wire ≈1 cm from the channel, with a diameter of ≈1 mm. EMIM TFSI is drop cast (≈50 µL) over the channel to gate the device.

In Figure 3b, we examine the output characteristics of the MoS_2 knot-based fiber transistor at gate voltages of 3, 0, and −3 V. These curves are consistent with our previous MoS_2 fibers showing n-type behavior and turn off at negative V_g (black curve), shown as a drop in I_d (<3 mA at 1 V_{ds}). In addition, we find our average transistor $\mu \approx 0.7 \pm 0.3\ cm^2\ V^{-1}\ s^{-1}$ from the slope in the linear region of the transfer characteristic, shown in Figure 3c, which is comparable to our previous MoS_2 fiber devices but with a reduction of $I_{on}/I_{off} \approx 10$ potentially due to charge screening. As an additional step toward decreasing the channel length, we fabricate an additional MoS_2 transistor with the knot architecture using the same manufacturing protocol but replacing the polyester for a human hair with ⌀ = 70 µm. Like the muti-fibril polyester fiber, we observe a homogeneous coating of MoS_2 flakes around the circumference of the fiber (Figure 3d) and conformal flake-to-flake junctions (Figure 3d) from SEM images. In this case, $L = 2\times⌀ = 140$ µm and $W = n\pi⌀ = 220$ µm since $n = 1$. Therefore, we find $\mu \approx 15 \pm 6\ cm^2\ V^{-1}\ s^{-1}$ and $I_{on}/I_{off} \approx 26 \pm 4$ from the transfer characteristic shown in Figure 3f. We find a sizeable improvement in μ likely due to the reduced transistor dimensions of L and W. Despite the reduction in I_{on}/I_{off} the architecture represents a potential route to decrease L_c and increase μ by shrinking the transistor geometry and reducing the number of flake-to-flake junctions, the limiting factor in flake networks. In this case, resolution is limited by our manual (by hand) assembly of the structure, however, it might be possible to decrease L_c further by using thinner fiber diameters such as electrospun fibers[60] using machine-based assembly with this architecture. A smaller fiber diameter might also help reduce parasitic channel resistance and charge screening, improving device performance. Although small diameter fibers (⌀ < 10 µm) are out of the scope of this work, the fabrication of high mobility $\mu > 10\ cm^2\ V^{-1}\ s^{-1}$ fiber transistors with TMD flakes represents an important first step for the field.

2.4. Biocompatibility of TMD Inks

The cytotoxic effect of TMD flakes on human cell lines after EE with QAS is largely unknown and can vary depending on concentration, shape, exposure time, functionalization, and cell line being tested.[61,62] LPE flakes of MoS_2 have demonstrated low cytotoxicity with a keratinocyte cell line for at least 48 h.[63] Conversely, the viability (using a colorimetric assay) of human lung carcinoma epithelial cells drops up to 60% after 24 h of exposure to MoS_2 flakes produced by EE using Li-intercalation.[64] Therefore, as a further investigation, we investigate the biocompatibility of our MoS_2 and WSe_2 flakes as the first steps to enable real-world applications of the electronic fibers that may be exposed near human skin. For example, the electrochemical transistors could be used in future work as sensors in human-machine interfaces in liquid environments and detect biological signals (e.g. analyte monitoring).[65] We choose keratinocytes to model the skin sub-surface. Before testing, the WSe_2 and MoS_2 inks are solvent-exchanged into deionized water (see Experimental Section). The keratinocyte cell bodies and nuclei are stained with phalloidin and DAPI and fluorescently imaged (see Experimental Section). In **Figure 4a,b**, the DNA content and cell metabolic activity were monitored after 80 µg mL^{-1} MoS_2 and 60 µg mL^{-1} WSe_2 ink addition for 24 and 72 h, respectively. No significant change in the DNA content and metabolic activity per DNA content was observed, indicating the biocompatibility of the MoS_2 and WSe_2 flakes for at least 72 h. WSe_2 also showed a potentially beneficial effect on the viability of the keratinocytes, with an increase in DNA content and metabolic activity per cell for the WSe_2-treated

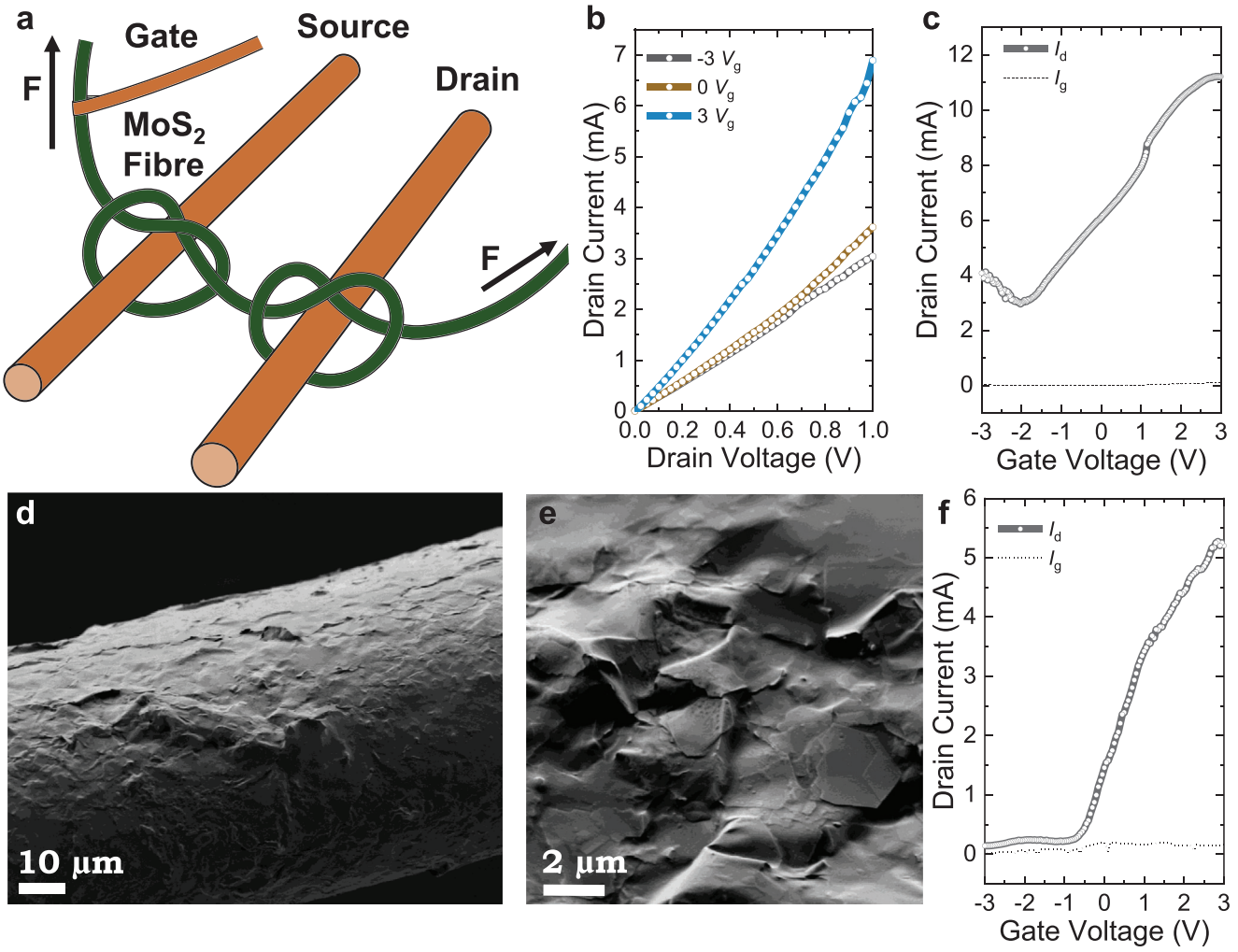

Figure 3. Investigation of knot architecture fiber transistors and their electrical properties. a) Schematic of fiber knot fiber transistor showing the MoS_2 coated fibers in green and the copper electrodes in brown. A force (F) is applied by hand in the direction of the arrows to tighten the MoS_2 fiber around the source and drain electrodes. b) Output characteristic of a MoS_2 knot fiber transistor. c) Transfer characteristics of the MoS_2 knot fiber transistor with the gate leakage shown as a dashed line. d) SEM of a human hair with MoS_2 flakes coated onto the circumference e) Magnified area of the MoS_2 coating on the human hair showing conformal flake-to-flake junctions f) Transfer characteristic of the human hair transistor using the knot architecture. Gate leakage is shown as the dashed line.

cells, possibly due to the presence of selenium which is an essential element for keratinocyte function.[66] Fluorescence imaging of the cells (see Experimental Section) after 3 days in culture with the MoS_2 (Figure 4c) and WSe_2 (Figure 4d) flakes at concentrations between 40 - 80 µg mL^{-1} yields cells with robust proliferation and healthy cellular morphology confirmed by the high nuclei count (Figure 4e) and area fraction (i.e. area covered by the cells) (Figure 4f). Finally, to simulate the longer-term interaction of cells with a TMD, keratinocytes are cultured with MoS_2 for 14 days. Fluorescent imaging demonstrats robust proliferation of the cells, with healthy cellular morphology (Figure 4g) that was similar to the media-only control (Figure 4h).

3. Conclusion

We find that high aspect ratio (AR >100) TMD flakes will self-align on polyester fiber after drop casting and make conformal flake-to-flake junctions that enable flexible high-mobility electronic networks $\mu \approx 15$ cm^2 V^{-1} s^{-1}, which has previously not been possible with TMDs in a fiber structure. MoS_2 fiber transistors are also demonstrated to be operational at a high tensile strain ≈4%, a key advantage of 2D materials and an essential requirement for wearable devices. We propose a novel 'knot' architecture, a lithography-free and textile-compatible method of manufacture to scale down future fiber transistors to the length scale of twice the fiber diameter and demonstrate its operation with both multifibril polyester fibers and human hair. As a final demonstration, electrochemical exfoliation of TMDs with QAS is also biocompatible with human skin cells. Keratinocytes cultured with MoS_2 and WSe_2 shows high viability, proliferation, and healthy cellular morphology over three days in culture and 14 days in culture for MoS_2. Therefore, the TMDs are suitable candidates for electronic fibers that may come into contact with human skin broadening their impact

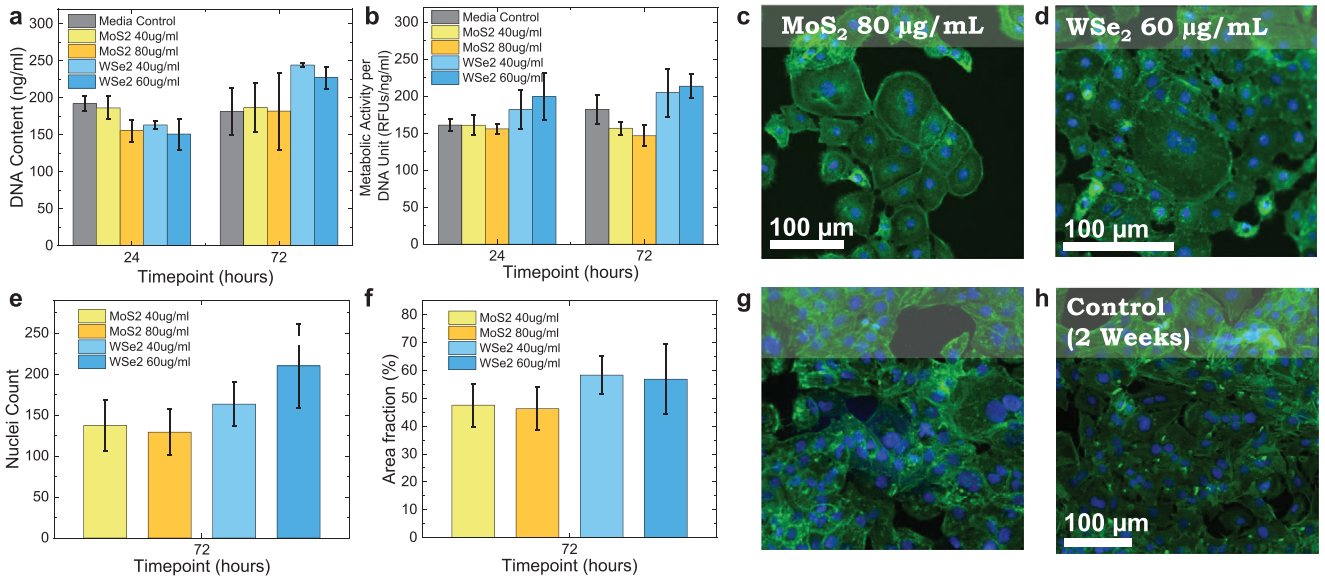

Figure 4. Biocompatibility testing of TMDs. a) Quantification of the DNA content as a function of time. b) Quantification of the metabolic activity per DNA unit as a function of time. c,d) Phalloidin (green) and DAPI (blue) stained HaCaT keratinocytes after 72 h growth in suspension with 80 µg mL^{-1} MoS_2 and 60 µg mL^{-1} WSe_2. e,f) Nuclei count and cell coverage found from microscopy after 72 h. g) Fluorescence image of keratinocytes grown in suspension with MoS_2 after 14 days of growth. h) Fluorescence image of keratinocytes with no addition of TMD's after 14 days of growth. Error is calculated by mixed effects analysis and 2-way ANOVA with Dunnett multiple comparisons where $n = 3$ (see Experimental Section for full details).

in enhancing the integration of electronics with human daily life.

4. Experimental Section

Electrochemical Exfoliation of 2D Crystals: To intercalate WSe_2 and MoS_2 (HQ graphene) crystals, a two-electrode electrochemical cell was utilized. The cathode was a thin piece of crystal measuring 0.1 × 1 × 1 mm, while a platinum foil from Alfa Aesar served as the anode. The electrodes were held in place with copper crocodile clips. The electrolyte consists of 5 mg mL^{-1} tetrapropylammonium (TPA) bromide from Sigma–Aldrich added to 50 mL of propylene carbonate. A voltage of 8 V was applied between the electrodes for 30 min to intercalate the 2D crystal with TPA+ cations. The expansion of the 2D crystal to more than twice its original volume in each case confirms the successful intercalation of the crystal.

Ink Formulation with 2D Crystals: The expanded 2D crystal undergoes bath sonication (Fisherbrand 112xx series) using 1 mg mL^{-1} PVP with a molecular weight of ≈40,000 dispersed in DMF for 5 min. Afterward, the mixture was centrifuged using a Hettich Mikro 220, with a radius of 87 mm, at 500 rpm (24g) for 20 min to remove unexfoliated crystals. The dispersion was then size-selected by centrifuging the supernatant (top 90%) at 1000 rpm (97g) for 1 h and collecting the sediment. To eliminate the PVP, the 97g sediment was diluted with 2 mL of DMF and centrifuged at 10,000 rpm (9744g). This process was repeated twice, and the sediment was collected each time. A third washing step was implemented to remove residual DMF, in which the sediment was diluted in IPA (0.5 mL) and centrifuged at 10,000 rpm (9744g), and the sediment was collected. The sediment was then redispersed in IPA (≈0.5 mL) with a concentration of ≈2.5 mg mL^{-1} for each crystal to create the MoS_2 and WSe_2 inks, respectively.

X-Ray Diffraction: XRD spectra were captured using a PanAlytical X'Pert Pro diffractometer with a Cu tube emitting Kα radiation (1.5406 Å). The spectra were acquired in the 2θ range from 10° to 90° on the flake networks prepared on Si/SiO_2 (100) orientated wafers (≈2000 nm oxide thickness).

Transmission Electron Microscopy: TEM lacey carbon grids were prepared for imaging by drop-casting the MoS_2 and WSe_2 inks and leaving them to dry overnight. A JEOL 2100 TEM was used for imaging the grids with a 200 kV accelerating voltage and 105 µA beam current.

Scanning Electron Microscopy: SEM imaging was conducted using a Carl Zeiss Ultra SEM. A secondary electron detector was used to obtain the images at a 1 and 3 kV accelerating voltage and 30 µm aperture.

FIB-SEM Cross-Section Imaging: FIB-SEM microscopy was carried out using a dual-beam Carl Zeiss Auriga focused ion beam system. A platinum pad was deposited by dissociation of a organometallic gas by the electron beam. Network cross-sections were milled with a 30 kV:120 pA gallium ion beam. All images were captured using the in-lens detector with an accelerating voltage of 2 kV and a 30 µm aperture at a working distance of 5 mm. The flake network thickness was averaged from 18 measurements at different points along the coated fiber.

Electrical Measurements: EMIM TFSI (Sigma–Aldrich) was employed as an ionic liquid to control ion injection into the semiconducting channel. The ionic liquid was heated at 70 °C under a vacuum (≈1.6 × 10^{-4} mbar) overnight on Si/SiO_2 to remove any water that might have been absorbed. The ionic liquid EMIM was then drop cast across the fiber, covering the gate, source, and drain electrodes. The devices were connected to a Keithley 2612A dual-channel source measurement unit employing gold-coated probes in ambient air to conduct electrical characterization. A scan rate of 50 mV s^{-1}, V_{ds} = 1 V, and a gate voltage window of −3 to 3 V were used to assess the transfer characteristics.

Atomic Force Microscopy: AFM was conducted to measure the flakes' thickness and lateral dimensions using a Bruker Multimode 8 microscope. Before imaging the MoS_2 and WSe_2 inks were diluted (1:100) in IPA and drop-cast onto Si/SiO_2. The samples were then annealed for 15 min at 120 °C in a Ar glovebox (UNIlab Pro, Mbraun) to remove any leftover solvent. The samples were scanned using the OLTESPA R3 cantilevers in ScanAsyst mode, 25 flakes were chosen for statistical analysis.

Raman Spectroscopy: Inks of MoS_2 and WSe_2 were drop cast onto Si/SiO_2 substrate and annealed at 120 °C. A WITec Raman spectrometer at 532 nm with a 20× objective was used to acquire spectra. An incident power of ≈1 mW was used to minimize possible thermal damage.

Optical Absorption Spectroscopy: A 10 mm optical length quartz cuvette and a Cary 1050 spectrometer were used to produce the spectra. The absorption spectra were collected in an integrating sphere. The collected extinction and absorption spectra of nanosheet dispersions were

subtracted by their corresponding IPA spectra to yield flake-only spectra. The scattering spectra were obtained by using extinction spectra and subtracting absorption spectra.

Human-Hair Transistors: A hair sample was obtained from a willing volunteer, and written consent from the participant was obtained prior to the research.

Biological Testing: The WSe_2 and MoS_2 inks were centrifuged at 10,000 rpm (9744g), and the IPA supernatant was decanted. The sediment was then redispersed in deionized water (≈0.5 mL) and centrifuged at 10,000 rpm (9744g) to remove residual IPA. The IPA/water supernatant was decanted, and the sediment was redispersed in deionized water (≈0.5 mL) at 2.5 mg mL^{-1} concentration. HaCaT keratinocytes were cultured in suspension with 40, 60, or 80 µg mL^{-1} of the respective TMD, diluted in growth media (low glucose Dulbecco's Modified Eagle Medium, 1% penicillin/streptomycin, 1% l-glutamine and 10% fetal bovine serum (FBS)). The metabolic activity was assessed by the Alamar Blue assay (Invitrogen, UK), and the DNA content was assessed by the Picogreen assay (Invitrogen, UK) on days 1 and 3. Cells were fixed using 10% formalin in PBS on days 3 and 14. Cells were subsequently stained with phalloidin to label the cell membrane, DAPI to label the nucleus, and fluorescently imaged on a Zeiss AxioObserver microscope to investigate the cell morphologies. Analysis of cell counts and area fraction was carried out using FIJI.[67]

Stress–Strain and Bending Tests: Tensile measurements were carried out with a Zwick Z0.5 ProLine Universal Testing Machine (100 N Load Cell) at a strain rate of 1% per second. All samples had a gauge length, L_0 = 20 mm, and were placed under a 500 kPa pre-load to ensure fibers were taught at the start of the measurement. For the MoS_2 FET bending tests, the device (⌀ ≈200 µm) was mounted on PET (thickness = 140 µm) with Kapton tape and bent using a fixed bending radius of 2.5 and 5 mm, respectively, strained parallel to the channel. Tensile strain (ϵ) was equal to $y/2r$, where r is the bending radius and y is the sample thickness.

Statistical Analysis: The data presented for the AFM flake lateral size and thickness uses the standard deviation of the mean (SDOM) where n = 25, TEM of network thickness uses SDOM with n = 10, mechanical data in Figure 4d uses SDOM with n = 3, transistor electrical data due to random error uses SDOM with n = 3. Error on the channel length assumes a systematic human error of 25% (i.e. the diameter of the copper wire) when manually placing the electrodes. The combined error on mobility due to batch variation and error due to the channel length estimation have been estimated using fractional propagation of error. For biological tests, the metabolic activity and metabolic activity per DNA content measurements use 2-way ANOVA with Dunnett multiple comparisons where n = 3, DNA content measurements use mixed-effects analysis with Dunnett's multiple comparisons where N = 3 for 24 h and N = 2 for 72 h. In all biological samples, $p > 0.05$. OriginPro was used for all graph plotting.

Supporting Information

Supporting Information is available from the Wiley Online Library or from the author.

Acknowledgements

The authors acknowledge the European Commission (Graphene Flagship Core 3 grant agreement No. 881603, respectively), the European Research Council (FUTURE-PRINT) and the Horizon Europe project 2D-PRINTABLE. The authors have also received support from the Science Foundation Ireland (SFI) funded center AMBER (SFI/12/RC/2278_P2) and availed of the facilities of the SFI-funded AML and ARL labs. C.I. acknowledges financial support of the Ministry of Education of Turkey and AMBER (Trinity College Dublin). T.C. acknowledge funding from a Marie Skłodowska-Curie Individual Fellowship "MOVE" (grant number 101030735, project number 211395, and award number 16883). E. C acknowledges funding from the Irish Reseach Council (GOIPG/2020/1051).

Conflict of Interest

The authors declare no conflict of interest.

Author Contributions

T.C. conceived and designed the experiments. T.C. manufactured inks and devices, *I–V* measurements, AFM, Raman Spectroscopy, and Optical Microscopy. S.L. took all UV–vis measurements. E.C. and L.D. did SEM measurements on fibers, L.D. undertook cross-sectional imaging. H.K. did all TEM of the TMD flakes. J.G. undertook stress–strain testing of the fibers. J.M. did all the biological testing. C.I. undertook XRD measurements. S.S. analyzed data and discussed the results. The manuscript was written by T.C. in close consultation with other authors.

Data Availability Statement

The data that support the findings of this study are available from the corresponding author upon reasonable request.

Keywords

2D materials, fiber electronics, transistors

Received: November 30, 2023
Revised: March 26, 2024
Published online:

[1] A. Birenboim, N. Shoval, *Ann. Assoc. Am. Geogr.* **2016**, *106*, 283.
[2] J. Hayward, E-Textiles 2019-2029: Technologies, Markets and Players, IDTechEx **2019**.
[3] S. Seyedin, T. Carey, A. Arbab, L. Eskandarian, S. Bohm, J. M. Kim, F. Torrisi, *Nanoscale* **2021**, *13*, 12818.
[4] H. C. Ates, P. Q. Nguyen, L. Gonzalez-Macia, E. Morales-Narváez, F. Güder, J. J. Collins, C. Dincer, *Nat. Rev. Mater.* **2022**, *7*, 887.
[5] J. Ren, C. Wang, X. Zhang, T. Carey, K. Chen, Y. Yin, F. Torrisi, *Carbon* **2017**, *111*, 622.
[6] Y. Peng, W. Li, B. Liu, W. Jin, J. Schaadt, J. Tang, G. Zhou, G. Wang, J. Zhou, C. Zhang, Y. Zhu, W. Huang, T. Wu, K. E. Goodson, C. Dames, R. Prasher, S. Fan, Y. Cui, *Nat. Commun.* **2021**, *12*, 6122.
[7] H. W. Choi, D.-W. Shin, J. Yang, S. Lee, C. Figueiredo, S. Sinopoli, K. Ullrich, P. Jovančić, A. Marrani, R. Momentè, J. Gomes, R. Branquinho, U. Emanuele, H. Lee, S. Y. Bang, S.-M. Jung, S. D. Han, S. Zhan, W. Harden-Chaters, Y.-H. Suh, X.-B. Fan, T. H. Lee, M. Chowdhury, Y. Choi, S. Nicotera, A. Torchia, F. M. Moncunill, V. G. Candel, N. Durães, K. Chang, et al., *Nat. Commun.* **2022**, *13*, 814.
[8] W. Zeng, X.-M. Tao, S. Chen, S. Shang, H. L. W. Chan, S. H. Choy, *Energy Environ. Sci.* **2013**, *6*, 2631.
[9] K. Dong, X. Peng, Z. L. Wang, *Adv. Mater.* **2020**, *32*, 1902549.
[10] M. Hatamvand, E. Kamrani, M. Lira-Cantú, M. Madsen, B. R. Patil, P. Vivo, M. S. Mehmood, A. Numan, I. Ahmed, Y. Zhan, *Nano Energy* **2020**, *71*, 104609.
[11] T. Carey, S. Cacovich, G. Divitini, J. Ren, A. Mansouri, J. M. Kim, C. Wang, C. Ducati, R. Sordan, F. Torrisi, *Nat. Commun.* **2017**, *8*, 1202.
[12] M. Hamedi, R. Forchheimer, O. Inganäs, *Nat. Mater.* **2007**, *6*, 357.
[13] D. De Rossi, *Nat. Mater.* **2007**, *6*, 328.
[14] Z. Wen, M.-H. Yeh, H. Guo, J. Wang, Y. Zi, W. Xu, J. Deng, L. Zhu, X. Wang, C. Hu, L. Zhu, X. Sun, Z. L. Wang, *Sci. Adv.* **2016**, *2*, e1600097.
[15] R. E. Owyeung, T. Terse-Thakoor, H. Rezaei Nejad, M. J. Panzer, S. R. Sonkusale, *ACS Appl. Mater. Interfaces* **2019**, *11*, 31096.

[16] C. Müller, M. Hamedi, R. Karlsson, R. Jansson, R. Marcilla, M. Hedhammar, *Adv. Mater.* **2011**, *23*, 898.
[17] S. J. Kim, H. Kim, J. Ahn, D. K. Hwang, H. Ju, M.-C. Park, H. Yang, S. H. Kim, H. W. Jang, J. A. Lim, *Adv. Mater.* **2019**, *31*, 1900564.
[18] J. S. Heo, K. W. Lee, J. H. Lee, S. B. Shin, J. W. Jo, Y. H. Kim, M. G. Kim, S. K. Park, *Micromachines* **2020**, *11*, 1103.
[19] B. Wang, A. Thukral, Z. Xie, L. Liu, X. Zhang, W. Huang, X. Yu, C. Yu, T. J. Marks, A. Facchetti, *Nat. Commun.* **2020**, *11*, 2405.
[20] C. J. Park, J. S. Heo, K.-T. Kim, G. Yi, J. Kang, J. S. Park, Y.-H. Kim, S. K. Park, *RSC Adv.* **2016**, *6*, 18596.
[21] M. Hamedi, L. Herlogsson, X. Crispin, R. Morcilla, M. Berggren, O. Inganäs, *Adv. Mater.* **2009**, *21*, 573.
[22] J. Rivnay, S. Inal, A. Salleo, R. M. Owens, M. Berggren, G. G. Malliaras, *Nat. Rev. Mater.* **2018**, *3*, 17086.
[23] P. Mittal, B. Kumar, Y. S. Negi, B. K. Kaushik, R. K. Singh, *Microelectron. J.* **2012**, *43*, 985.
[24] H. M. Kim, H. W. Kang, D. K. Hwang, H. S. Lim, B.-K. Ju, J. A. Lim, *Adv. Funct. Mater.* **2016**, *26*, 2706.
[25] G. Mattana, P. Cosseddu, B. Fraboni, G. G. Malliaras, J. P. Hinestroza, A. Bonfiglio, *Org. Electron.* **2011**, *12*, 2033.
[26] S. Nam, J. Jang, J. J. Park, S. W. Kim, C. E. Park, J. M. Kim, *ACS Appl. Mater. Interfaces* **2012**, *4*, 6.
[27] M. Kang, S.-A. Lee, S. Jang, S. Hwang, S.-K. Lee, S. Bae, J.-M. Hong, S. H. Lee, K.-U. Jeong, J. A. Lim, T.-W. Kim, *ACS Appl. Mater. Interfaces* **2019**, *11*, 22575.
[28] J. B. Lee, V. Subramanian, *IEEE Trans. Electron Devices* **2005**, *52*, 269.
[29] M. Maccioni, E. Orgiu, P. Cosseddu, S. Locci, A. Bonfiglio, *Appl. Phys. Lett.* **2006**, *89*, 143515.
[30] W. Lee, Y. Kim, M. Y. Lee, J. H. Oh, J. U. Lee, *Org. Electron.* **2019**, *69*, 320.
[31] N. Münzenrieder, C. Vogt, L. Petti, G. A. Salvatore, G. Cantarella, L. Büthe, G. Tröster, *Technologies* **2017**, *5*, 31.
[32] S. Hwang, M. Kang, A. Lee, S. Bae, S.-K. Lee, S. H. Lee, T. Lee, G. Wang, T.-W. Kim, *Nat. Commun.* **2022**, *13*, 3173.
[33] Q. Huang, J. Wang, C. Li, J. Zhu, W. Wang, Y. Huang, Y. Zhang, H. Jiao, S. Zhang, H. Meng, M. Zhang, X. Wang, *npj Flexible Electron.* **2022**, *6*, 61.
[34] Z. Zhu, N. Wei, W. Cheng, B. Shen, S. Sun, J. Gao, Q. Wen, R. Zhang, J. Xu, Y. Wang, F. Wei, *Nat. Commun.* **2019**, *10*, 4467.
[35] A. F. Paterson, S. Singh, K. J. Fallon, T. Hodsden, Y. Han, B. C. Schroeder, H. Bronstein, M. Heeney, I. McCulloch, T. D. Anthopoulos, *Adv. Mater.* **2018**, *30*, 1801079.
[36] T. Carey, A. Alhourani, R. Tian, S. Seyedin, A. Arbab, J. Maughan, L. Šiller, D. Horvath, A. Kelly, H. Kaur, E. Caffrey, J. M. Kim, H. R. Hagland, J. N. Coleman, *npj 2D Mater. Appl.* **2022**, *6*, 3.
[37] T. Carey, O. Cassidy, K. Synnatschke, E. Caffrey, J. Garcia, S. Liu, H. Kaur, A. G. Kelly, J. Munuera, C. Gabbett, D. O'Suilleabhain, J. N. Coleman, *ACS Nano* **2023**, *17*, 2912.
[38] Z. Lin, Y. Liu, U. Halim, M. Ding, Y. Liu, Y. Wang, C. Jia, P. Chen, X. Duan, C. Wang, F. Song, M. Li, C. Wan, Y. Huang, X. Duan, *Nature* **2018**, *562*, 254.
[39] K. S. Novoselov, V. I. Fal'ko, L. Colombo, P. R. Gellert, M. G. Schwab, K. Kim, *Nature* **2012**, *490*, 192.
[40] F. Torrisi, T. Carey, *Nano Today* **2018**, *23*, 73.
[41] A. G. Kelly, T. Hallam, C. Backes, A. Harvey, A. S. Esmaeily, I. Godwin, J. Coelho, V. Nicolosi, J. Lauth, A. Kulkarni, S. Kinge, L. D. Siebbeles, G. S. Duesberg, J. N. Coleman, *Science* **2017**, *356*, 69.
[42] A. G. Kelly, D. O'Suilleabhain, C. Gabbett, J. N. Coleman, *Nat. Rev. Mater.* **2021**, *7*, 217.
[43] D. O'Suilleabhain, A. G. Kelly, R. Tian, C. Gabbett, D. Horvath, J. N. Coleman, *ACS Appl. Electron. Mater.* **2020**, *2*, 2164.
[44] T. M. Higgins, S. Finn, M. Matthiesen, S. Grieger, K. Synnatschke, M. Brohmann, M. Rother, C. Backes, J. Zaumseil, *Adv. Funct. Mater.* **2019**, *29*, 1804387.
[45] T. Carey, C. Jones, F. Le Moal, D. Deganello, F. Torrisi, *ACS Appl. Mater. Interfaces* **2018**, *10*, 19948.
[46] Y. Li, K. Chang, Z. Sun, E. Shangguan, H. Tang, B. Li, J. Sun, Z. Chang, *ACS Appl. Energy Mater.* **2020**, *3*, 998.
[47] Y. J. Park, H.-S. So, H. Hwang, D. S. Jeong, H. J. Lee, J. Lim, C. G. Kim, H. S. Shin, *ACS Nano* **2022**, *16*, 11059.
[48] M. Wu, J. Zhan, K. Wu, Z. Li, L. Wang, B. Geng, L. Wang, D. Pan, *J. Mater. Chem. A* **2017**, *5*, 14061.
[49] P. Zaumseil, *J. Appl. Crystallogr.* **2015**, *48*, 528.
[50] X. Wang, X. Chen, Y. Zhou, C. Park, C. An, Y. Zhou, R. Zhang, C. Gu, W. Yang, Z. Yang, *Sci. Rep.* **2017**, *7*, 46694.
[51] K. Fujisawa, B. R. Carvalho, T. Zhang, N. Perea-Lopez, Z. Lin, V. Carozo, S. Ramos, E. Kahn, A. Bolotsky, H. Liu, A. L. Elias, M. Terrones, *ACS Nano* **2021**, *15*, 9658.
[52] M. S. Sokolikova, P. C. Sherrell, P. Palczynski, V. L. Bemmer, C. Mattevi, *Nat. Commun.* **2019**, *10*, 712.
[53] E. Er, H.-L. Hou, A. Criado, J. Langer, M. Möller, N. Erk, L. M. Liz-Marzán, M. Prato, *Chem. Mater.* **2019**, *31*, 5725.
[54] C. Backes, R. J. Smith, N. McEvoy, N. C. Berner, D. McCloskey, H. C. Nerl, A. O'Neill, P. J. King, T. Higgins, D. Hanlon, N. Scheuschner, J. Maultzsch, L. Houben, G. S. Duesberg, J. F. Donegan, V. Nicolosi, J. N. Coleman, *Nat. Commun.* **2014**, *5*, 4576.
[55] W. Zhao, Z. Ghorannevis, L. Chu, M. Toh, C. Kloc, P. H. Tan, G. Eda, *ACS Nano* **2013**, *7*, 791.
[56] G. Gunduz, D. Erol, N. Akkas, *J. Compos. Mater.* **2005**, *39*, 1577.
[57] J. Kim, M. Jung, D. U. Lim, D. Rhee, S. H. Jung, H. K. Cho, H. K. Kim, J. H. Cho, J. Kang, *Nano Lett.* **2022**, *22*, 570.
[58] R. A. Wells, M. Zhang, T.-H. Chen, V. Boureau, M. Caretti, Y. Liu, J.-H. Yum, H. Johnson, S. Kinge, A. Radenovic, K. Sivula, *ACS Nano* **2022**, *16*, 5719.
[59] E. Piatti, A. Arbab, F. Galanti, T. Carey, L. Anzi, D. Spurling, A. Roy, A. Zhussupbekova, K. A. Patel, J. M. Kim, D. Daghero, R. Sordan, V. Nicolosi, R. S. Gonnelli, F. Torrisi, *Nat. Electron.* **2021**, *4*, 893.
[60] J. A. Merlo, C. D. Frisbie, *J. Polym. Sci., Part B: Polym. Phys.* **2003**, *41*, 2674.
[61] C.-X. Hu, O. Read, Y. Shin, Y. Chen, J. Wang, M. Boyes, N. Zeng, A. Panigrahi, K. Kostarelos, I. Larrosa, S. Vranic, C. Casiraghi, *ACS Appl. Nano Mater.* **2022**, *5*, 12626.
[62] C. Martín, K. Kostarelos, M. Prato, A. Bianco, *Chem. Commun.* **2019**, *55*, 5540.
[63] J. Kaur, M. Singh, C. Dell'Aversana, R. Benedetti, P. Giardina, M. Rossi, M. Valadan, A. Vergara, A. Cutarelli, A. M. I. Montone, L. Altucci, F. Corrado, A. Nebbioso, C. Altucci, *Sci. Rep.* **2018**, *8*, 16386.
[64] E. L. K. Chng, Z. Sofer, M. Pumera, *Nanoscale* **2014**, *6*, 14412.
[65] S. T. Keene, D. Fogarty, R. Cooke, C. D. Casadevall, A. Salleo, O. Parlak, *Adv. Healthcare Mater.* **2019**, *8*, 1901321.
[66] A. Sengupta, U. F. Lichti, B. A. Carlson, A. O. Ryscavage, V. N. Gladyshev, S. H. Yuspa, D. L. Hatfield, *PLoS One* **2010**, *5*, e12249.
[67] J. Schindelin, I. Arganda-Carreras, E. Frise, V. Kaynig, M. Longair, T. Pietzsch, S. Preibisch, C. Rueden, S. Saalfeld, B. Schmid, J.-Y. Tinevez, D. J. White, V. Hartenstein, K. Eliceiri, P. Tomancak, A. Cardona, *Nat. Methods* **2012**, *9*, 676.

